Discrete Equivalent Wing Crack based Damage Model for Brittle Solids

Wencheng Jin[a], Chloé Arson[a,*]

[a]*School of Civil and Environmental Engineering, Georgia Institute of Technology, USA*

Abstract

The Discrete Equivalent Wing Crack Damage (DEWCD) model formulated in this paper couples micro-mechanics and Continuum Damage Mechanics (CDM) principles. At the scale of the Representative Elementary Volume (REV), damage is obtained by integrating crack densities over the unit sphere, which represents all possible crack plane orientations. The unit sphere is discretized into 42 integration points. The damage yield criterion is expressed at the microscopic scale: if a crack is in tension, crack growth is controlled by a mode I fracture mechanics criterion; if a crack is in compression, the shear stress that applies at its faces is projected on the directions considered in the numerical integration scheme, and cracks perpendicular to these projected force components grow according to a mode I fracture mechanics criterion. The projection of shear stresses into a set of tensile forces allows predicting the occurrence of wing cracks at the tips of pre-existing defects. We assume that all of the resulting mode I cracks do not interact, and we adopt a dilute homogenization scheme. A hardening law is introduced to account for subcritical crack propagation, and non-associated flow

*Corresponding author

Email address: chloe.arson@ce.gatech.edu (Chloé Arson)

rules are adopted for damage and irreversible strains induced by residual crack displacements after unloading. The DEWCD model depends on only 6 constitutive parameters which all have a sound physical meaning and can be determined by direct measurements in the laboratory. The DEWCD model is calibrated and validated against triaxial compression tests performed on Bakken Shale. In order to highlight the advantages of the DEWCD model over previous anisotropic damage models proposed for rocks, we simulated: (a) A uniaxial tension followed by unloading and reloading in compression; and (b) Uniaxial compression loading cycles of increasing amplitude. We compared the results obtained with the DEWCD model with those obtained with a micro-mechanical model and with a CDM model, both calibrated against the same experimental dataset as the DEWCD model. The three models predict a non linear-stress/strain relationship and damage-induced anisotropy. The micro-mechanical model can capture unilateral effects. The CDM model can capture the occurrence of irreversible strains. The DEWCD model can capture both unilateral effects and irreversible strains. In addition, the DEWCD model can predict the apparent increase of strength and ductility in compression when the confinement increases and the increasing hysteresis on unloading-reloading paths as damage increases. The DEWCD model is the only of the three models tested that provides realistic values of yield stress and strength in tension and compression. This is a significant advancement in the theoretical modeling of brittle solids. Future work will be devoted to the prediction of crack coalescence and to the modeling of the material response with interacting micro-cracks.

Keywords: Continuum Damage Mechanics, Micromechanics, Anisotropic

1. Introduction

In most brittle materials such as rocks, concrete and ceramic composites, mechanical failure is the result of a sequence of coupled micro-processes. In Continuum Damage Mechanics (CDM), anisotropic damage is usually represented by second-order tensors (Murakami, 1988; Halm and Dragon, 1996) or fourth-order tensors (Ju, 1989) that depend on the density and orientation of families of micro-cracks. The expression of the damaged stiffness tensor is based on the principle of strain or energy equivalence (Murakami, 2012), and stress/strain relationships are deduced from the thermodynamic relationships that are derived from the energy potentials. The damage flow rule, combined with the consistency condition, allows determining the evolution of the magnitude and direction of micro-cracks (Simo and Ju, 1987; Chaboche, 1993; Hayakawa and Murakami, 1997). CDM models were implemented in Finite Element Methods (FEM) for practical engineering purposes (e.g., (Jin et al., 2015; Xu and Arson, 2015; Jin et al., 2016)) and were successfully used to predict damage-induced anisotropy and confinement-induced strengthening in rock subject to compression (e.g., (Shao and Rudnicki, 2000; Shao et al., 2005, 2006)), as well as unilateral effects (e.g., (Chaboche, 1993; Dragon et al., 2000)). However, multiple non-linear damage phenomena require more constitutive parameters that are often not related to any microstructure or mechanical property, which raises calibration challenges (Halm and Dragon, 1996, 1998; Arson, 2014). Moreover, difficulties arise when distinguishing tension and compression: either the stress or the strain tensor has to be

split into positive and negative components. Damage evolution depends on distinct yield criteria and damage potentials (Lubarda et al., 1994; Frémond and Nedjar, 1996; Comi and Perego, 2001; Zhu and Arson, 2013). These so called bi-dissipative models are based on complex mathematical formulations (challenging to implement in FEM) and depend on a large number of parameters (challenging to calibrate). In micromechanical models, a direct relationship is established between the macroscopic mechanical behavior and micro-crack initiation, propagation, opening, closure and frictional sliding. In the dilute crack scheme, the calculation of the displacement jump across crack faces (Budiansky and O'connell, 1976) is used as a basis to upscale the effective properties of the damaged REV (Kachanov, 1992, 1993) and to express the corresponding energy potentials (Kachanov, 1982a,b; Pensée et al., 2002; Pensee and Kondo, 2003). The evolution law is based on fracture mechanics and can represent Mode I splitting (Krajcinovic et al., 1991; Gambarotta and Lagomarsino, 1993), Mode II friction sliding (Gambarotta and Lagomarsino, 1993) or mixed Mode wing crack development (Kachanov, 1982b; Nemat-Nasser and Obata, 1988). In order to account for crack interactions, one can explicitly express the stress field that results from external loading and crack interaction (Paliwal and Ramesh, 2008). Other upscaling techniques (e.g., (Zhu et al., 2008, 2009; Zhu and Shao, 2015; Qi et al., 2016a,b)) resort to Eshelby homogenization procedure (Eshelby, 1957), in which the cracked solid is viewed as a matrix-inclusion system (Dormieux et al., 2006). Micromechanical formulations automatically predict unilateral effects but usually cannot capture the inelastic deformation together with the softening that characterize the REV behavior after the peak of stress, and

they require computationally intensive resolution algorithms. In this paper, we formulate an anisotropic damage model that couples micro-mechanical crack propagation criteria and CDM energy principles with a minimum number of constitutive parameters. In Section 2, we present the theoretical formulation of our model, called the Discrete Equivalent Wing Crack based Damage model (DEWCD). A finite number of orientations is used to project the normal and tangential crack displacement vectors. The damage variable is a second-order crack density tensor, and the irreversible deformation is the crack opening vector averaged over all possible crack orientations. In tension, cracks propagate in mode I in the direction normal to the tensile stress. In compression, wing cracks propagate in mode I in the direction of the minimum deviatoric stress. We calibrate and validate the DEWCD model against triaxial compression data obtained on Middle Bakken shale. In Section 3, we use the same experimental dataset to calibrate a phenomenological damage model, the Differential-Stress Induced Damage (DSID) model (Xu and Arson, 2014, 2015) and a micromechanical damage model (Pensée et al., 2002; Pensee and Kondo, 2003). We simulate: (1) A uniaxial tension followed by unloading and uniaxial compression; and (2) Two loading-unloading cycles of uniaxial compression of increasing amplitude. We compare the performance of the three models for capturing damage-induced anisotropy of stiffness, unilateral effects in compression, damage hysteresis during unloading-reloading cycles, damage-induced irreversible strains, confinement-dependent strength, and differences of behavior in tension and compression.

2. Theoretical Formulation of the Discrete Equivalent Wing Crack Damage (DEWCD) model

2.1. Micromechanics-based free enthalpy

We formulate a CDM model in which the expression of the free enthalpy is obtained from micromechanics principles. In the following, we consider a REV of volume Ω_r and external boundary $\partial\Omega_r$, in which a large number of penny shaped microscopic cracks of various orientations are embedded in an isotropic linear elastic matrix of compliance tensor $\mathbb{S}_0$. Each microscopic crack is characterized by its normal direction $\overrightarrow{n}$ and its radius a, which is at least 100 times smaller than the REV size. Opposite crack faces are noted ω^+ and ω^-, with normal vectors $\overrightarrow{n}^+$ and $\overrightarrow{n}^-$. The displacement jump is noted:

$$[\overrightarrow{u}] = \overrightarrow{u}^+ - \overrightarrow{u}^- \tag{1}$$

Where $\overrightarrow{u}^+$ (respectively $\overrightarrow{u}^-$) denotes the displacement vector at face ω^+ (respectively ω^-). We consider a uniform stress field $\boldsymbol{\sigma}$ applied at the boundary $\partial\Omega_r$. The displacement field at the REV scale is calculated by superposition, by adding up the displacement field in the elastic matrix in the absence of cracks and the displacement field induced by the opening and sliding of micro-crack faces.

We assume that the mechanical interaction between cracks is negligible and we use a dilute homogenization scheme to calculate the crack displacement jumps. As a result, the average micro stress is equal to the stress field applied to the REV, so that we have:

$$\boldsymbol{\sigma} = \frac{1}{|\Omega_r|}\int_{\Omega_r}[\boldsymbol{\sigma}^m(\boldsymbol{x}) + \boldsymbol{\sigma}^c(\boldsymbol{x})]\mathrm{d}\boldsymbol{x} \tag{2}$$

In which $\boldsymbol{\sigma}^c$ is the stress field that is applied at micro-crack faces and $\boldsymbol{\sigma}^m$ is the stress field in the linear elastic matrix. Moreover, the local stress at crack faces is self-equilibrating, so that:

$$\frac{1}{|\Omega_r|}\int_{\Omega_r}\boldsymbol{\sigma}^c(\boldsymbol{x})\mathrm{d}\boldsymbol{x}=0 \tag{3}$$

And therefore:

$$\boldsymbol{\sigma}=\langle\boldsymbol{\sigma}^m\rangle \tag{4}$$

The strain tensor in the matrix is obtained as follows:

$$\boldsymbol{\epsilon}^m=\mathbb{S}_0:\boldsymbol{\sigma}. \tag{5}$$

Each micro-crack can be considered as a single crack embedded in an infinite elastic homogeneous matrix, which allows calculating the displacement jumps from fracture mechanics principles (Horii and Nemat-Nasser, 1983; Kachanov et al., 2013). Considering a penny shaped crack of radius a subjected to a uniformly distributed normal stress p at its faces and embedded in an infinite elastic medium with Young's modulus E_0 and Poisson's ratio ν_0, the normal displacement jump is:

$$[u_n]=8\frac{1-\nu_0^2}{\pi E_0}p\sqrt{a^2-r^2} \tag{6}$$

The corresponding average Crack Opening Displacement (COD) is therefore:

$$\langle[u_n]\rangle=\frac{16}{3}\frac{1-\nu_0^2}{\pi E_0}pa \tag{7}$$

Similarly, considering a penny shaped crack of radius a subjected to a uniformly distributed shear stress $\overrightarrow{\tau}$ at its faces and embedded in an infinite

elastic medium with Young's modulus E_0 and Poisson's ratio ν_0, the shear displacement jump is expressed as (Kachanov et al., 2013):

$$\langle[\overrightarrow{u_t}]\rangle = \frac{32}{3}\frac{1-\nu_0^2}{(2-\nu_0)\pi E_0}\overrightarrow{\tau}a \tag{8}$$

We first consider a REV that contains a single family of N cracks of same orientation $\overrightarrow{n_i}$ and same size a_i. The volume fraction of the normal and shear displacement jumps are calculated as follows:

$$\begin{aligned}\beta_i &= \frac{N}{|\Omega_r|}\langle[u_n]\rangle\pi(a_i)^2 = \rho_i c_0 \boldsymbol{\sigma}^c : (\overrightarrow{n_i}\otimes\overrightarrow{n_i}) \\ \overrightarrow{\gamma_i} &= \frac{N}{|\Omega_r|}\langle[\overrightarrow{u_t}]\rangle\pi(a_i)^2 = \rho_i c_1(\boldsymbol{\sigma}^c\cdot\overrightarrow{n_i} - (\overrightarrow{n_i}\cdot\boldsymbol{\sigma}^c\cdot\overrightarrow{n_i})\overrightarrow{n_i})\end{aligned} \tag{9}$$

Where $p = \boldsymbol{\sigma}^c : (\overrightarrow{n_i}\otimes\overrightarrow{n_i})$, $\overrightarrow{\tau} = \boldsymbol{\sigma}^c\cdot\overrightarrow{n_i} - (\overrightarrow{n_i}\cdot\boldsymbol{\sigma}^c\cdot\overrightarrow{n_i})\overrightarrow{n_i}$ and ρ_i is the damage density along the direction $\overrightarrow{n_i}$, expressed as:

$$\rho_i = \frac{Na^3}{|\Omega_r|} \tag{10}$$

The coefficient c_0 (respectively c_1) is defined as the normal (respectively shear) elastic compliance of the crack (Budiansky and O'connell, 1976; Kachanov, 1992):

$$\begin{aligned}c_0 &= \frac{16}{3}\frac{1-\nu_0^2}{E_0} \\ c_1 &= \frac{32}{3}\frac{1-\nu_0^2}{(2-\nu_0)E_0}\end{aligned} \tag{11}$$

According to the dilute homogenization scheme, the average strain due to the crack r is calculated as:

$$\langle\boldsymbol{\epsilon}^{c,r}\rangle = \frac{1}{2|\Omega_r|}\int_{\partial\omega^+}(\overrightarrow{n}\otimes[\overrightarrow{u}] + [\overrightarrow{u}]\otimes\overrightarrow{n})\mathrm{d}S \tag{12}$$

As a result, the overall average strain due to the entire family of micro-cracks of normal $\overrightarrow{n_i}$ can be obtained by summation, as follows:

$$\begin{aligned}\boldsymbol{\epsilon}^c &= \frac{N}{|\Omega_r|}\int_{\partial\omega^+}[u_n](\overrightarrow{n_i}\otimes\overrightarrow{n_i})\mathrm{d}S \\ &\quad + \frac{N}{2|\Omega_r|}\int_{\partial\omega^+}([\overrightarrow{u_t}]\otimes\overrightarrow{n_i}+\overrightarrow{n_i}\otimes[\overrightarrow{u_t}])\mathrm{d}S \\ &= \beta_i\overrightarrow{n_i}\otimes\overrightarrow{n_i}+\frac{1}{2}(\overrightarrow{\gamma_i}\otimes\overrightarrow{n_i}+\overrightarrow{n_i}\otimes\overrightarrow{\gamma_i})\end{aligned} \tag{13}$$

With $[u_n] = [\overrightarrow{u}]\cdot\overrightarrow{n_i}$ and $[\overrightarrow{u_t}] = [\overrightarrow{u}] - [u_n]\overrightarrow{n_i}$. The free energy W^* of the REV containing the N cracks of orientation $\overrightarrow{n_i}$ is the sum of the elastic deformation energy of the matrix and the energy stored in the micro cracks displacement jumps:

$$W^* = \frac{1}{2}\boldsymbol{\epsilon}^m : \mathbb{C}_0 : \boldsymbol{\epsilon}^m + \frac{1}{2}\boldsymbol{\sigma}^c : \boldsymbol{\epsilon}^c \tag{14}$$

Now substituting Eq.9 and Eq.13 into the above equation, the Helmholtz free energy W^* of the REV can be rewritten as:

$$\begin{aligned}W^* &= \frac{1}{2}\boldsymbol{\epsilon}^m : \mathbb{C}_0 : \boldsymbol{\epsilon}^m + \frac{1}{2}\boldsymbol{\sigma}^c : [\beta_i\overrightarrow{n_i}\otimes\overrightarrow{n_i}+\frac{1}{2}(\overrightarrow{\gamma_i}\otimes\overrightarrow{n_i}+\overrightarrow{n_i}\otimes\overrightarrow{\gamma_i})] \\ &= \frac{1}{2}\boldsymbol{\epsilon}^m : \mathbb{C}_0 : \boldsymbol{\epsilon}^m + \frac{1}{2\rho_i c_0}\beta_i^2 + \frac{1}{2\rho_i c_1}\overrightarrow{\gamma_i}\cdot\overrightarrow{\gamma_i}\end{aligned} \tag{15}$$

The Gibbs energy (free enthalpy) is obtained by Legendre transformation, as follows:

$$G^* = \boldsymbol{\sigma} : \boldsymbol{\epsilon}^E - W^* \tag{16}$$

In which $\boldsymbol{\epsilon}^E = \boldsymbol{\epsilon}^m + \boldsymbol{\epsilon}^c$ is the REV elastic strain. As a result, G^* is expressed as:

$$\begin{aligned}G^* &= \frac{1}{2}\boldsymbol{\sigma} : \mathbb{S}_0 : \boldsymbol{\sigma} + \boldsymbol{\sigma} : \boldsymbol{\epsilon}^c - \frac{1}{2}\boldsymbol{\sigma}^c : \boldsymbol{\epsilon}^c \\ &= \frac{1}{2}\boldsymbol{\sigma} : \mathbb{S}_0 : \boldsymbol{\sigma} + \boldsymbol{\sigma} : [\beta_i\overrightarrow{n_i}\otimes\overrightarrow{n_i}+\frac{1}{2}(\overrightarrow{\gamma_i}\otimes\overrightarrow{n_i}+\overrightarrow{n_i}\otimes\overrightarrow{\gamma_i})] \\ &\quad - \frac{1}{2\rho_i c_0}\beta_i^2 - \frac{1}{2\rho_i c_1}\overrightarrow{\gamma_i}\cdot\overrightarrow{\gamma_i}\end{aligned} \tag{17}$$

For a reversible process, i.e. for a fixed crack density, we have:

$$\begin{aligned}\dot{G}^* &= \boldsymbol{\epsilon}^E : \dot{\boldsymbol{\sigma}} \\ 0 &= [\boldsymbol{\sigma} : (\overrightarrow{n_i} \otimes \overrightarrow{n_i}) - \frac{1}{\rho_i c_0}\beta_i]\dot{\beta}_i + [(\boldsymbol{\sigma} \cdot \overrightarrow{n_i} - (\overrightarrow{n_i} \cdot \boldsymbol{\sigma} \cdot \overrightarrow{n_i})\overrightarrow{n_i}) \\ &\quad - \frac{1}{\rho_i c_1}\overrightarrow{\gamma_i}] \cdot \dot{\overrightarrow{\gamma_i}}\end{aligned} \tag{18}$$

From which we get:

$$\begin{aligned}\boldsymbol{\sigma} : (\overrightarrow{n_i} \otimes \overrightarrow{n_i}) &= \frac{1}{\rho_i c_0}\beta_i \\ \boldsymbol{\sigma} \cdot \overrightarrow{n_i} - (\overrightarrow{n_i} \cdot \boldsymbol{\sigma} \cdot \overrightarrow{n_i})\overrightarrow{n_i} &= \frac{1}{\rho_i c_1}\overrightarrow{\gamma_i} \cdot \dot{\overrightarrow{\gamma_i}}\end{aligned} \tag{19}$$

According to the dilute homogenization scheme, the equivalent traction at the crack faces (at the REV scale) is given by:

$$\overrightarrow{t_i} = \boldsymbol{\sigma}^c \cdot \overrightarrow{n_i} \tag{20}$$

A normal displacement jump can only be induced by a tensile force, i.e. for $\overrightarrow{n_i} \cdot \boldsymbol{\sigma} \cdot \overrightarrow{n_i} \leq 0$ (in which compression is counted positive, according to the soil mechanics convention). The unilateral contact condition at crack faces can be expressed as

$$[u_n] \geq 0, \quad \sigma_{nn} = \overrightarrow{n} \cdot \boldsymbol{\sigma} \cdot \overrightarrow{n} \leq 0, \quad [u_n]\sigma_{nn} = 0 \tag{21}$$

Using the conjugation relationships in Eq. 19 in the expression of free enthalpy in Eq.17 and introducing the unilateral condition, we get:

$$\begin{aligned}G^* =& \frac{1}{2}\boldsymbol{\sigma} : \mathbb{S}_0 : \boldsymbol{\sigma} + \frac{1}{2}c_0\rho_i(\overrightarrow{n_i} \cdot \boldsymbol{\sigma} \cdot \overrightarrow{n_i})\langle\overrightarrow{n_i} \cdot \boldsymbol{\sigma} \cdot \overrightarrow{n_i}\rangle^+ \\ &+ \frac{1}{2}c_1\rho_i[(\boldsymbol{\sigma} \cdot \boldsymbol{\sigma}) : (\overrightarrow{n_i} \otimes \overrightarrow{n_i}) - \boldsymbol{\sigma} : (\overrightarrow{n_i} \otimes \overrightarrow{n_i} \otimes \overrightarrow{n_i} \otimes \overrightarrow{n_i}) : \boldsymbol{\sigma}]\end{aligned} \tag{22}$$

In which we note $\langle x\rangle^+ = x, x \geq 0$, and $\langle x\rangle^+ = 0, x < 0$. The Gibbs energy of the REV is obtained by integrating G^* for a distribution of crack orientations $\rho(n)$, over the unit sphere $S^2 = \{\overrightarrow{n}, |\overrightarrow{n}| = 1\}$, as follows:

$$\begin{aligned} G =& \frac{1}{2}\boldsymbol{\sigma} : \mathbb{S}_0 : \boldsymbol{\sigma} + \frac{1}{8\pi}\int_{S^2}\{c_0\,\rho(\overrightarrow{n})(\overrightarrow{n}\cdot\boldsymbol{\sigma}\cdot\overrightarrow{n})\langle\overrightarrow{n}\cdot\boldsymbol{\sigma}\cdot\overrightarrow{n}\rangle^+ \\ &+ c_1\,\rho(\overrightarrow{n})[(\boldsymbol{\sigma}\cdot\boldsymbol{\sigma}) : (\overrightarrow{n}\otimes\overrightarrow{n}) - \boldsymbol{\sigma} : (\overrightarrow{n}\otimes\overrightarrow{n}\otimes\overrightarrow{n}\otimes\overrightarrow{n}) : \boldsymbol{\sigma}]\}\mathrm{d}S \end{aligned} \tag{23}$$

Because the calculation of the integral above is impractical for a continuous distribution $\rho(\overrightarrow{n})$, we use a numerical integration scheme, with M integration points:

$$\begin{aligned} G =& \frac{1}{2}\boldsymbol{\sigma} : \mathbb{S}_0 : \boldsymbol{\sigma} + \frac{1}{2}\sum_{i=1}^{M} w_i\{c_0\rho_i(\overrightarrow{n_i}\cdot\boldsymbol{\sigma}\cdot\overrightarrow{n_i})\langle\overrightarrow{n_i}\cdot\boldsymbol{\sigma}\cdot\overrightarrow{n_i}\rangle^+ \\ &+ c_1\rho_i[(\boldsymbol{\sigma}\cdot\boldsymbol{\sigma}) : (\overrightarrow{n_i}\otimes\overrightarrow{n_i}) - \boldsymbol{\sigma} : (\overrightarrow{n_i}\otimes\overrightarrow{n_i}\otimes\overrightarrow{n_i}\otimes\overrightarrow{n_i}) : \boldsymbol{\sigma}]\} \end{aligned} \tag{24}$$

Where w_i is the weight in direction n_i. We adopt Bazant's discrete scheme with 2×21 microplanes (Bažant and Oh, 1986). Note that the calculation of G requires M calculations at each time step. Increasing M can increase exponentially the computational cost of the numerical integration. Bazant's 2×21 scheme provides satisfactory accuracy at reasonable computation cost. For a detailed discussion about the performance of numerical integration scheme, the reader is referred to (Ehret et al., 2010; Levasseur et al., 2013).

The expression of Gibbs energy expressed in Eq. 24 accounts for the displacement field induced by crack opening and crack sliding, but not for crack growth (i.e., the model does not account for the increase of crack radius). In order to account for inelastic crack dedonding (i.e. crack radius growth), we introduce the inelastic strain $\boldsymbol{\epsilon}^{in}$ in the formulation. We adopt a hyper-elastic framework (Collins and Houlsby, 1997), in which the REV strain tensor $\boldsymbol{\epsilon}$

is split into a pure elastic part $\boldsymbol{\epsilon}^e$ which corresponds to the deformation of elastic matrix, an additional elastic part $\boldsymbol{\epsilon}^d$ which represents the micro-crack elastic strain, and the inelastic deformation $\boldsymbol{\epsilon}^{in}$, as follows:

$$\boldsymbol{\epsilon} = \boldsymbol{\epsilon}^e + \boldsymbol{\epsilon}^d + \boldsymbol{\epsilon}^{in} = \boldsymbol{\epsilon}^E + \boldsymbol{\epsilon}^{in} \tag{25}$$

In which:

$$\begin{aligned} \boldsymbol{\epsilon}^e &= \frac{1+\nu_0}{E_0}\boldsymbol{\sigma} - \frac{\nu_0}{E_0}\mathrm{Tr}(\boldsymbol{\sigma})\boldsymbol{\delta} \\ \boldsymbol{\epsilon}^d &= \sum_{i=1}^{M} w_i\{c_0\rho_i\langle\overrightarrow{n_i}\cdot\boldsymbol{\sigma}\cdot\overrightarrow{n_i}\rangle^+\overrightarrow{n_i}\otimes\overrightarrow{n_i} \\ &\quad + c_1\rho_i[\boldsymbol{\sigma}\cdot(\overrightarrow{n_i}\otimes\overrightarrow{n_i}) - (\overrightarrow{n_i}\cdot\boldsymbol{\sigma}\cdot\overrightarrow{n_i})\overrightarrow{n_i}\otimes\overrightarrow{n_i}]\} \end{aligned} \tag{26}$$

Conjugation relationships can be established to calculate the total elastic strain $\boldsymbol{\epsilon}^E$ and the damage driving force Y_i:

$$\boldsymbol{\epsilon}^E = \boldsymbol{\epsilon}^e + \boldsymbol{\epsilon}^d = \frac{\partial G}{\partial \boldsymbol{\sigma}} \tag{27}$$

$$\begin{aligned} Y_i = \frac{\partial G}{\partial \rho_i} =& \frac{1}{2}w_i\{c_0(\overrightarrow{n_i}\cdot\boldsymbol{\sigma}\cdot\overrightarrow{n_i})\langle\overrightarrow{n_i}\cdot\boldsymbol{\sigma}\cdot\overrightarrow{n_i}\rangle^+ \\ &+ c_1[(\boldsymbol{\sigma}\cdot\boldsymbol{\sigma}) : (\overrightarrow{n_i}\otimes\overrightarrow{n_i}) - \boldsymbol{\sigma} : (\overrightarrow{n_i}\otimes\overrightarrow{n_i}\otimes\overrightarrow{n_i}\otimes\overrightarrow{n_i}) : \boldsymbol{\sigma}]\} \end{aligned} \tag{28}$$

2.2. Damage yield criterion

Uniaxial compression tests performed on two-dimensional photoelastic materials highlighted the occurrence of two wing cracks at the tips of pre-existing cracks. Wing cracks propagate along a curved path, of average direction parallel to the direction of maximum compression (Nemat-Nasser and Horii, 1982; Ashby and Hallam, 1986; Horii and Nemat-Nasser, 1986). The sliding wing crack model was initially presented in the pioneering work

of Bombolakis and Brace (Bombolakis and Brace, 1963). Since then, numerous studies were devoted to the mechanisms of crack propagation in brittle solids under compression, for instance: (Nemat-Nasser and Horii, 1982; Ashby and Hallam, 1986; Horii and Nemat-Nasser, 1986; Dyskin and Salganik, 1987; Nemat-Nasser and Obata, 1988; Lehner and Kachanov, 1996). 3D lab experiments (Germanovich et al., 1994; Sahouryeh et al., 2002), numerical simulations (Scholtès and Donzé, 2012) and theoretical derivations (Dyskin and Salganik, 1987) were also proposed to model the propagation of tensile wing cracks at the tip of sliding cracks ('slips'). Friction forces at the faces of slips are thus the forces driving the propagation of wing cracks. 3D wing cracks propagate due to mixed failure modes (I, II or III) at different locations along the edge of the pre-exiting slip cracks. The shape of 3D wing cracks is therefore extremely complex, and depends on a high number of parameters.

For practicality, we ignore friction at crack faces, i.e. we assume that wing cracks propagate in pure mode I and we represent the propagation of shear cracks in the form of tensile wing cracks. We ignore the interaction between these tensile micro-cracks and we apply the dilute hogenization scheme. If the unilateral contact condition is satisfied, cracks propagate due to normal tensile stresses, according to the following mode I propagation criterion:

$$f_d(\boldsymbol{\sigma}, a_i) = \sigma^i_{nn} - \frac{K_c}{\sqrt{a_i}} \tag{29}$$

Where K_c is a constitutive parameter which represents the material toughness. We define the second-order crack density tensor $\boldsymbol{\Omega}$ (also called second-

order damage tensor) as follows:

$$\boldsymbol{\Omega} = \sum_{i=1}^{M} \rho_i \overrightarrow{n_i} \otimes \overrightarrow{n_i}. \tag{30}$$

If the unilateral contact condition is not satisfied, shear stresses at the faces of slip cracks induce the propagation of wing cracks. Following (Horii and Nemat-Nasser, 1986; Lehner and Kachanov, 1996), we represent two half wing cracks as a single fictitious circular crack, as shown in Fig.1.

The direction of maximum shear stress at the faces of the cracks perpendicular to direction $\overrightarrow{n_i}$ can be calculated as follows:

$$\overrightarrow{m_i} = \frac{\tau^c}{||\tau^c||} = \frac{\boldsymbol{\sigma} \cdot \overrightarrow{n_i} - (\overrightarrow{n_i} \cdot \boldsymbol{\sigma} \cdot \overrightarrow{n_i})\overrightarrow{n_i}}{||\boldsymbol{\sigma} \cdot \overrightarrow{n_i} - (\overrightarrow{n_i} \cdot \boldsymbol{\sigma} \cdot \overrightarrow{n_i})\overrightarrow{n_i}||} \tag{31}$$

We solve the wing crack propagation problem in two dimensions, by assuming that the normal of the equivalent fictitious circular crack that represents the wing cracks is contained in the plane (m_i, n_i). Therefore, we have:

$$\begin{aligned} \sigma^i_{nn} &= \overrightarrow{n_i} \cdot \boldsymbol{\sigma} \cdot \overrightarrow{n_i} \\ \tau^i_{nm} &= ||\boldsymbol{\sigma} \cdot \overrightarrow{n_i} - (\overrightarrow{n_i} \cdot \boldsymbol{\sigma} \cdot \overrightarrow{n_i})\overrightarrow{n_i}|| \\ \sigma^i_{mm} &= \overrightarrow{m_i} \cdot \boldsymbol{\sigma} \cdot \overrightarrow{m_i} \end{aligned} \tag{32}$$

The tensile force F applied at the faces of the fictitious wing crack is equal to the shear forces undergone by the pre-existing 'slip' of radius a_i, and can be calculated as:

$$F = \pi a_i^2 \tau^c = \pi a_i^2 \tau^i_{nm} \tag{33}$$

Experimental (Sahouryeh et al., 2002) and numerical (Scholtès and Donzé, 2012) studies indicate that wing cracks propagate along the direction of maximum compression stress. When the pre-existing 'slip' crack is in compression

and subjected to shear stresses, the normal to the fictitious planar crack representing the wing cracks is therefore oriented in the direction of minimum compression (Eq.32). Using Mohr's circles, the intensity σ_{min} and direction θ_i of the mimimum compression are calculated as follows:

$$\begin{aligned} tan(2\theta_i) &= \frac{2\tau^i_{nm}}{\sigma^i_{mm} - \sigma^i_{nn}} \\ \sigma_{min} &= \frac{\sigma^i_{mm} + \sigma^i_{nn}}{2} - \sqrt{(\frac{\sigma^i_{mm} - \sigma^i_{nn}}{2})^2 + (\tau^i_{nm})^2} \end{aligned} \tag{34}$$

Based on the theory of linear fracture mechanics, we consider that the wing crack propagates only if the stress intensity factor reaches the material toughness. Assuming that the tensile driving force F is uniformly distributed along the faces of the fictitious planar crack (Fig.1), we define the wing micro crack propagation criterion as follows:

$$f_{d0}(\boldsymbol{\sigma}, a_{\theta i}) = \sqrt{\pi\, a_{\theta i}} \left(\frac{F cos(\theta_i)}{\pi a^2_{\theta i}} - \sigma_{min} \right) - K_c \sqrt{\pi} \tag{35}$$

Satisfying the criterion f_{d0} is equivalent to satisfying the following criterion, which will be adopted in the following for wing crack propagation:

$$f_d(\boldsymbol{\sigma}, a_{\theta i}) = \left(cos(\theta_i) \tau^i_{nm} (\frac{a_i}{a_{\theta i}})^2 - \sigma_{min} \right) - \frac{K_c}{\sqrt{a_{\theta i}}} \tag{36}$$

$a_{\theta i}$ is the radius of the fictitious wing crack, which can be determined by projecting the damage tensor defined in Eq. 30 as follows:

$$a_{\theta i} = (\frac{|\Omega_r|}{N} \overrightarrow{n_\theta} \cdot \boldsymbol{\Omega} \cdot \overrightarrow{n_\theta})^{1/3} \tag{37}$$

$\overrightarrow{n_\theta}$ is the unit vector normal to the family of wing cracks of orientation θ, and is expressed as:

$$\overrightarrow{n_\theta} = \overrightarrow{m_i} cos(\theta_i) + \overrightarrow{n_i} sin(\theta_i) \tag{38}$$

The progressive stiffness degradation observed before the peak of stress in experimental rock mechanics compression tests indicates that wing micro-cracks propagate in a stable way (Yuan and Harrison, 2006). Theoretically, in the subcritical regime, cracks can propagate even when the stress intensity factor is lower than the material toughness. Moreover, the stress intensity required for crack propagation increases as the crack propagates (Savalli and Engelder, 2005). In order to account for this hardening effect, we propose to express the material toughness as a hyperbolic function of the crack radius, as follows:

$$K_c = \frac{a^{3/2}}{\frac{1}{K_0} + \frac{a}{\sigma_c}} \tag{39}$$

Where $a = a_{\theta i}$ for a crack in compression (leading to the propagation of wing cracks), and $a = a_i$ for a crack in tension. As shown in Fig.2, the yield point depends on K_0, the slope of the plot that represents the variations the toughness with the square root of the fracture length. The parameter σ_c controls the peak driving force that the REV can sustain.

2.3. Damage potential and flow rule

Inelastic strains observed after unloading are due to residual geometric incompatibilities at the crack faces, which depend on the damage-driving forces Y_i. The micro-crack propagation criteria formulated in Eq. 29 and 36 depend on stress and cannot properly represent the occurrence of residual displacement fields after unloading. We thus derive the evolution laws of inelastic strains from non associate flow rules. We introduce discrete damage potentials (expressed in terms of Y_i) in a homogeneous function of degree

one, as follows:

$$g_d(n_i) = Y_i - C_0 \tag{40}$$

Following a non-associate flow rule, the inelastic strain increment can be computed from the damage potential as

$$\begin{aligned}\dot{\boldsymbol{\epsilon}}^{in} &= \sum_{i=1}^{M} \dot{\lambda}_i \frac{\partial g_d(n_i)}{\partial \boldsymbol{\sigma}} = \sum_{i=1}^{M} \dot{\lambda}_i \frac{\partial Y_i}{\partial \boldsymbol{\sigma}} \\ &= \sum_{i=1}^{M} w_i \dot{\lambda}_i \{ c_0 \langle \overrightarrow{n_i} \cdot \boldsymbol{\sigma} \cdot \overrightarrow{n_i} \rangle^{+} \overrightarrow{n_i} \otimes \overrightarrow{n_i} \\ &\quad + c_1 [\boldsymbol{\sigma} \cdot (\overrightarrow{n_i} \otimes \overrightarrow{n_i}) - (\overrightarrow{n_i} \cdot \boldsymbol{\sigma} \cdot \overrightarrow{n_i}) \overrightarrow{n_i} \otimes \overrightarrow{n_i}] \}\end{aligned} \tag{41}$$

Where λ_i is Lagrange multiplier for each family of crack with normal $\overrightarrow{n_i}$. Similarly, the increment of damage density is calculated as:

$$\dot{\rho}_i = \dot{\lambda}_i \frac{\partial g_d}{\partial Y_i} = \dot{\lambda}_i \tag{42}$$

The incremental damage density is calculated from the increments of crack radius, as follows:

$$\Delta \rho_i = \frac{N}{|\Omega_r|} \Delta(a_i^3) \tag{43}$$

In which $\Delta(a_i^3)$ represents the variation of the value of a_i^3 between two iterations. We have: $\Delta(a_i^3) = 3(a_i)^2 \Delta(a_i)$ in which $\Delta(a_i)$ is obtained by using the consistency rule:

$$\Delta(a_i) = -\frac{\frac{\partial f_d}{\partial \boldsymbol{\sigma}}}{\frac{\partial f_d}{\partial a_i}} \, : \, \Delta \boldsymbol{\sigma} \tag{44}$$

The equation above requires calculating the derivatives of τ_{nm}^i and σ_{min} with respect to the stress tensor $\boldsymbol{\sigma}$, which is computationally intensive. We employ

the Newton iteration scheme to update the radius of the micro cracks at each load step. As shown in Fig.3, the tangent of the yield criterion is calculated at each iteration i to approach the exact crack size at load step n+1, as follows:

$$a_{n,i+1} = a_{n,i} - \frac{f_d(\boldsymbol{\sigma}_{n,i}, a_{n,i})}{f'_d(\boldsymbol{\sigma}_{n,i}, a_{n,i})} \tag{45}$$

The convergence criterion ($r_{n,i}$) is expressed as

$$||r_{n,i}|| = ||a_{n,i+1} - a_{n,i}|| \leq \epsilon_{TOL} \tag{46}$$

Where ϵ_{TOL} is a tolerance value. Once the increment of crack radius is obtained for each crack orientation ($\Delta(a_i)$, $\Delta(a_{\theta i})$), the increment of damage tensor $\Delta\boldsymbol{\Omega}$ can be updated as

$$\Delta\boldsymbol{\Omega} = \sum_{i=1}^{M} \frac{N}{|\Omega_r|} \Delta({a_i}^3) \overrightarrow{n_i} \otimes \overrightarrow{n_i} + \sum_{i=1}^{M} \frac{N}{|\Omega_r|} \Delta({a_{\theta i}}^3) \overrightarrow{n_{\theta_i}} \otimes \overrightarrow{n_{\theta_i}} \tag{47}$$

In the equation above, the variation of crack density in direction $\overrightarrow{n_i}$ accounts for the growth of cracks perpendicular to direction $\overrightarrow{n_i}$ in mode I, and for the growth of wing cracks that develop at the tips of cracks that are not perpendicular to $\overrightarrow{n_i}$. The proposed model is named Discrete Equivalent Wing Crack based Damage (DEWCD) model because frictional wing cracks are indirectly represented by equivalent tensile wing cracks obtained by projection. The DEWCD model is designed to capture splitting and crossing effects. We used the quadrature rules explained above (Bažant and Oh, 1986) to project the vectors $\overrightarrow{n_{\theta_i}}$ on the 42 directions $\overrightarrow{n_i}$. Ultimately, the increment of crack density is obtained by projecting the increment of damage tensor in each of the 42 directions considered in the quadrature:

$$\Delta\rho_i = \overrightarrow{n_i} \cdot \Delta\boldsymbol{\Omega} \cdot \overrightarrow{n_i} \tag{48}$$

2.4. DEWCD Model calibration and validation

The Discrete Equivalent Wing Crack based Damage (DEWCD) model depends on six constitutive parameters: the reference (initial) Young's modulus E_0, the reference (initial) Poission's ratio ν_0, the reference (initial) microcrack radius a_0, the microcrack density (Number of crack per unit volume) $\mathbb{N} = \frac{N}{|\Omega_r|}$, the initial toughness slope K_0 and the critical stress σ_c. For an intrinsically anisotropic material (i.e. with anisotropy not induced by micro-crack propagation), the model can easily be adapted by choosing different values of reference radius (a_0) for different crack orientations. The six parameters above have a sound physical meaning and can be determined by performing standard mechanical tests (e.g., uniaxial and triaxial compression tests; uniaxial tension test; Brazilian test), and microstructure characterizations (e.g. Scanning Electron Microscopy; acoustic emissions). In the following, we calibrate and validate the DEWCD model against a series of triaxial compression tests performed on North Dakota Bakken shale plugs in ConocoPhillips rock mechanics laboratory. All the samples were dry (Amendt et al., 2013). Plugs were cored from the same depth and lithology and were selected to avoid major bedding discontinuities, and were considered homogeneous. We used the stress/strain curves obtained with a confinement of 2000 psi (13.8 MPa) for calibration, and we validated the model with confinements of 1000 psi (6.9 MPa) and 3000 psi (20.7 MPa). Note that the soil mechanics sign convention was adopted throughout the paper (with compression counted positive).

We used the Interior Point Algorithm programmed in MATLAB to determine the unknown vector $\boldsymbol{B} = (E_0, \nu_0, a_0, \mathbb{N}, K_0, \sigma_c)$ that minimizes the squared residual of the distance between experimental results y_i and numeri-

cal predictions $f_i(\boldsymbol{X}, \boldsymbol{B})$. The residual that is minimized iteratively is defined as:

$$R(\boldsymbol{B}) = \sum_{i=1}^{n} [y_i - f_i(\boldsymbol{X}, \boldsymbol{B})]^2 \tag{49}$$

Where $\boldsymbol{X}$ stands for the vector of known input variables (e.g., strain or stress, depending whether the load is controlled in force or displacement). The algorithm was initialized with an initial guess, as well as the lower bound and the upper bound of the coefficients of the unknown parameter vector $\boldsymbol{B}$. Then, triaxial compression tests were simulated with the DEWCD model at the material point, and the value of the residual $R(\boldsymbol{B})$ was calculated based on the set of parameters obtained at the previous iteration. The gradient of the residual $R(\boldsymbol{B})$ with respect to each parameter in the vector $\boldsymbol{B}$ was calculated and used to minimize the difference between numerical and experimental stress-strain curves, as follows:

$$\boldsymbol{B}_{n+1} = \boldsymbol{B}_n - \gamma_n \Delta R(\boldsymbol{B}) \tag{50}$$

Where γ_n is the barrier parameter, which is updated at each iteration step in the Interior Point Algorithm. The procedure is described in detail in (Byrd et al., 2000; Waltz et al., 2006).

Fig.4(a) shows the experimental stress-strain curve (green star marker) and the numerical stress-strain curve obtained after model calibration (green solid line) for a confinement of $\sigma_3 = 13.8$ MPa. Note that the calibration of the DEWCD model was based on experimental data obtained before the failure stress, because the DEWCD model does not capture the interactions and coalescence of cracks during the post peak softening regime. Curves match closely except for the lateral deformation, which is underestimated by

the DEWCD model for damage values higher than 10%. We interpret this discrepancy by the fact that shale is not a purely brittle material. Ductile deformation at high damage induces large lateral strains, which cannot be captured by the DEWCD model, especially for shales that contain significant amounts of clay/organic matter (Sone and Zoback, 2013a,b). We simulated the triaxial compression tests performed under confinements of $\sigma_3 = 6.9$ MPa (solid blue line) and $\sigma_3 = 20.7$ MPa (solid red line) using the calibrated parameters, and compared the DEWCD predictions with experimental data (blue circle markers and red square makers, respectively). Similar to the the theory of plasticity, we define the yield stress as the value of stress at which micro cracks start to propagate (damage initiation), and we define the the material strength as the peak value of stress in the stress/strain curve. Fig.4(a) shows that the DEWCD model captures the increase of the yield stress σ_y with increasing confining pressure σ_3. Over 800 sampling points were used on the experimental stress/strain curves before the failure peak to assess the accuracy of the model predictions after calibration. The error, defined as the distance between the numerical and experimental curves, is less than 5%, which is considered very satisfactory provided the unavoidable microstructural differences between the initial rock samples. Fig.4(b) shows the evolution of the principal values of the damage tensor for the three confining pressures considered. Micro-cracks normal to the axial direction of the compression load (x_1) are fully closed, therefore $\Omega_1 = 0$ in all tests. The lateral damage components Ω_2 and Ω_3 are induced by the opening of wing cracks at the tips of non horizontal cracks, which are subjected to local shear stresses. Lateral damage increases exponentially with

deviatoric stress. As the deviatoric stress approaches the value of the peak stress noted in the stress/strain curves, the tangent to the damage evolution curve approaches infinity. Physically, this phenomenon corresponds to strong micro-crack interactions leading to crack coalescence and macroscopic discontinuities. Overall, the performance of the DEWCD model for the calibrated parameters is very satisfactory. The DEWCD model parameters calibrated for North Dakota Bakken Shale are reported in Table 1. Using these calibrated model parameters, we simulated triaxial compression tests under confining pressures ranging from 5 MPa to 28 MPa. We calculated the deviatoric stress at which the Young's modulus was decreased to 25% of its initial value. As shown in Fig.5, the value of that threshold stress increases linearly with the confining pressure. Moreover, the variations of the threshold stress with the confining pressure match those of the compressive strength obtained experimentally. This indicates that the DEWCD allows predicting the failure (peak) stress.

3. Comparison of the DEWCD model with phenomenological and micromechanical damage models

In the following, we explain the theoretical formulation of a micromechanical model (Pensée et al., 2002; Pensee and Kondo, 2003) and of the phenomenological Differential Stress Induced Damage (DSID) model, and we calibrate the micro-mechanical and DSID models against the same experimental dataset as the DEWCD model. Then we compare the performance of the micro-mechanical, DSID and DEWCD models in capturing damage-induced anisotropy, crack-induced dilation strains, damage hystere-

sis, confinement-dependent strength, unilateral effects in compression, and distinct behaviors in tension and compression.

3.1. Formulation and calibration of the micro-mechanical damage model

Table 2 summarizes the main equations of the micro-mechanical model presented in (Pensée et al., 2002; Pensee and Kondo, 2003). The free enthalpy (Gibbs free energy) is the sum of the elastic deformation energy stored in the non-damaged matrix and of the potential energy due to the displacement jumps at the micro-crack faces. A discrete formulation is adopted, with M possible crack orientations characterized by a crack density and a unilateral condition. Crack closure is considered elastic. Crack debonding is the only dissipation mechanism considered in the model. Based on the assumption of crack non-interaction, damage ($\mathbf{\Omega}$) is defined as the crack density tensor (i.e. as the sum of crack densities projected in their respective crack directions). For each of the M micro-crack directions, the damage yield criterion is expressed as a linear hardening law, in terms of the crack density and of its work-conjugate energy release rate. Since the only dissipation mechanism adopted in the model is crack debonding, an associated damage flow rule is adopted.

We used the same triaxial compression test dataset obtained for North Dakota Middle Bakken Shale as in subsection 2.4 for micro-mechanical model clibration and validation (Tab. 3). Following the same procedure as in subsection 2.4, we use the experimental results obtained with a confining pressure of $\sigma_3 = 13.6$ MPa for calibration and the results obtained for confining pressures of $\sigma_3 = 6.9$ MPa and $\sigma_3 = 20.7$ MPa to verify the model parameters. As shown in Fig.6(a), the high initial stiffness is compensated by a high dam-

age propagation rate. Although the residual minimized by the calibration algorithm reaches a very low value, the stress/strain curve predicted by the micro-mechanical model does not match the experimental results satisfactorily, especially for the lateral deformation. The main micro-crack propagation mechanism is based on micro-crack face sliding under compression. During a triaxial compression test, the highest crack densities are those of cracks oriented by an angle of approximately 45 degrees from the loading axis. As a result, the axial damage component Ω_1 (crack planes parallel to the compression axis) is higher than the lateral damage components Ω_2 and Ω_3 (Fig.6(b)), which is counter-intuitive for a compression test. Fig.6 also shows that the stress/strain response predicted by the micro-mechanical model is the same for the three confining pressures investigated. This is because the damage yield criterion is expressed in terms of energy release rate, which is essentially controlled by deviatoric stress $\sigma_1 - \sigma_3$. As a result, the influence of the confining pressure on the damage yield stress cannot be captured by the micro-mechanical model.

3.2. Theoretical formulation and calibration of the phenomenological DSID model

The theoretical formulation of the DSID model (Xu and Arson, 2014, 2015) is summarized in Table 4. The damage tensor (noted $\boldsymbol{\Omega}$) is a phenomenological internal variable, which controls the degradation of material stiffness along principal crack planes. The free enthalpy (Gibbs free energy, G) is expressed as the sum of the damaged elastic deformation energy stored in the material, the potential energy that can be released by creating new material surfaces, and the potential energy that can be released by opening

cracks (i.e., the potential irreversible deformation energy). This free enthalpy potential is expressed as a polynomial that is quadratic in stress and linear in damage, which implies that the material is linear elastic in the absence of damage (Shao et al., 2005; Halm and Dragon, 1998). Stress/strain relationships are obtained by deriving the Gibbs energy by stress. Damage evolution is controlled by a damage function, similar to the Drucker-Prager yield function (but expressed in terms of energy release rate instead of stress). The damage flow rule is non-associate, and the damage potential is chosen so as to ensure the positivity of dissipation associated to damage. The irreversible deformation due to damage follows an associate flow rule, which ensures that dilation due to crack opening takes place in the damage principal directions (i.e. in the directions orthogonal to the crack planes).

Similar to the DEWCD model and the micro-mechanical damage models, we first calibrated the DSID model against experimental stress-strain curves obtained during a triaxial compression test performed under a confining pressure of $\sigma_3 = 13.8$ MPa, as shown in Fig.7(a). Unlike the micromechanical damage model, the phenomenological DSID model can predict the stress-strain curves before the occurrence of damage. However, like the micro-mechanical damage model, the DSID model fails at capturing large dilative lateral deformation. Fig.7(b) shows that lateral damage components Ω_2 and Ω_3, which correspond to crack planes parallel to the loading axis, propagate with increasing deviatoric stress, and that axial damage Ω_1 remains equal to zero, which is physically reasonable. However, the rate of damage propagation is very small, even at the peak stress. In other words, the DSID model predicts a continuous hardening even after the experimental

peak stress, which is not physically reasonable. As shown in the magnified part of Fig.7(b), the DSID model can capture the dependence of the yield stress to the confining pressure. This is conform to the yield criterion chosen in the DSID model, which depends on the confining stress through the term αI^*. However, the DSID model predicts that the material under high confining pressure softens faster, and yields a higher level of damage. This inconsistency is due to the unreasonable damage evolution predicted by the model and to the negligible difference in yield stress in the three triaxial compression tests. This problem can be overcome by calibrating the DSID model against the whole set of experimental data instead of just one stress strain curve (however, we calibrated the DSID model against the dataset obtained at a confining pressure of $\sigma_3 = 13.8$ MPa to match the calibration procedure used in the two other models).

3.3. Simulation of uniaxial tension followed by compression

One of the major characteristics of brittle solids such as rocks, concrete and ceramics, is that they yield at a very low tensile stress and fail soon after yielding. Before complete failure, stiffness damaged in tension can be partially recovered in compression, due to the unilateral effects of crack closure (Mazars et al., 1990). In order to assess the performance of the three damage models to capture tensile failure and unilateral effects, we simulated a uniaxial tension test followed by unloading and uniaxial compression. All simulations were done in MATLAB at the material point, with the model parameters calibrated above (Tab. 1, 3 and 5).

Figures 8(a) and 8(b) show that according to the micro-mechanical model the tensile yield stress of Bakken shale is $\sigma_y = 45$ MPa. This result is unreal-

istic for a rock material, because most rocks fail at that stress level in tension. This discrepancy is due to the fact that the projection of crack densities in the principal damage directions yields non zero lateral damage (Ω_2 and Ω_3), even in uniaxial tension. Moreover, the damage evolution rate for both lateral and axial damage components is very slow. The phenomenological DSID model gives a reasonable tensile yield stress of $\sigma_y = 15$ MPa (Fig.8(c)). However, the rate of damage propagation is slow and axial damage amounts to only 10% when the tensile stress reaches 60 MPa. According to the DSID model, Bakken shale follows an elastic behavior followed by hardening after the yield stress has been reached (Fig.8(d)). Figures 8(e) and 8(f) show that according to the DEWCD model, Bakken shale yields at $\sigma_y = 12$ MPa in uniaxial tension. After yielding, the damage propagation rate is high. Large inelastic strains accumulate in the axial direction (Fig.8(e)), which is unrealistic, because brittle solids subject to tensile loads tend to fail catastrophically without large deformation. That being said, crack interactions other than the occurrence of wing cracks are ignored in the DEWCD model, which is aimed to capture the damaged behavior before the peak of stress (Eq.24). After a certain level of damage, micro-crack interaction and coalescence cannot be neglected. In order to capture the transition between smeared and localized damage propagation, it would be more suitable to couple the DEWCD model to a model of fracture mechanics. For the sake of completeness, we show the results obtained for a tensile stress up to 45 MPa to compare the DEWCD model with the micro-mechanical and DSID models. We note that the introduction of a damage potential together with non-associate flow rules in the DSID and DEWCD models allows capturing

the occurrence of residual inelastic strains after unloading, which are not accounted for in the micro-mechanical model. Simulation results obtained with the micro-mechanical and DEWCD models also highlight unilateral effects induced by crack closure in compression, which are not captured by the DSID model.

Fig.9 shows the evolution of the energy potentials for a uniaxial tension simulation followed by unloading and uniaxial compression. Note that at any point, the external work input equals the sum of the elastic deformation energy stored in the REV and the dissipation potentials. Dissipation results solely from crack debonding in the micro-mechanical model. In the DSID model, the total work input is the sum of the purely elastic strain energy stored in the matrix, the additional damage-induced elastic strain energy (due to stiffness degradation), and the inelastic strain energy (due to residual crack-induced deformation). In the DEWCD model, elastic strain energy is stored in the matrix ('matrix elastic strain energy' in Fig. 9(c)) and between crack faces (displacement jumps - 'damage induced strain energy' in Fig. 9(c)), and energy is dissipated in the form of inelastic strain energy. The damage-induced strain energy is one order of magnitude larger in the DEWCD model than in the other two models, because of the significant damage growth rate predicted by the DEWCD model after the peak stress. By contrast with the micro-mechanical and DSID models, the DEWCD model predicts that the compressive strength of the initial material is higher than that of the material that has been damaged during the uniaxial tension loading stage: the compressive strength is about 50 MPa in the virgin material (Fig. 10(f)), while is it only 5 MPa in the presence of tensile damage (Fig.

8(f)).

3.4. Simulation of uniaxial compression cycles of increasing amplitude.

The compression strength of rock-like brittle solids is usually an order of magnitude larger than the tensile strength. Requirements of thermodynamic consistency (i.e. positive dissipation potentials) and yield function differentiability make it challenging to combine two different criteria in tension and compression. Some formulations split the stress into compressive and tensile components (Comi and Perego, 2001; Shao and Rudnicki, 2000); other models are based on the decomposition of strains into positive and negative parts (Dragon et al., 2000). In the DEWCD model, crack propagation in modes I and II are modeled with two mode I propagation criteria applied to two different categories of cracks (tensile crack propagation and tensile wing crack propagation). In order to assess the performance of this modeling strategy in distinguishing the yield and failure in tension and compression, we simulate a cyclic compressive loading path with the micro-mechanical, DSID and DEWCD models. Results obtained with the parameters calibrated above for Bakken shale are shown in Fig. 10.

In the micro-mechanical model studied here, the unconfined compressive yield stress is about 100 MPa (Fig. 10(a)-10(b)), which is an order of magnitude higher than the 45 MPa tensile yield stress found in the previous tests. With the DSID model, the unconfined compression strength is $\sigma_y = 40$ MPa, which is acceptable for a rock material (Fig. 10(c)-10(d)). However, the sample still does not fail under a uniaxial compressive stress of 250 MPa, which means that the uniaxial compressive strength predicted is more than 250 MPa: this is approximately twice as much as what was expected for shale.

From Fig.8(d), it can also be seen that more than 60 MPa uniaxial tension is required to achieve a 0.3 damage. According to Kachanov's calculations (Kachanov, 1992), a damage of 0.3 corresponds to the initiation of crack interactions, above which the framework of CDM is no longer valid and the REV has reached failure. Accordingly, the present simulations indicate that the tensile strength predicted by the DSID model exceeds 60 MPa, which is several times higher than the value expected for shale.

Contrary to the micro-mechanical and DSID models, the DEWCD model predicts values of yield stress and strength that are in the range of values expected for a rock material like shale (Fig. 10(e) and 10(f)). The yield stress predicted by the DEWCD model in uniaxial compression is 50 MPa. Damage reaches 0.3 for a uniaxial compression stress of 180 MPa, and for a uniaxial tensile stress of 30 MPa (Fig. 8(f) and 10(f)). For the compression test simulated with the DEWCD and DSID models, axial damage (crack planes perpendicular to the loading axis) does not propagate, and the lateral damage components grow exponentially after the yield stress is reached, which is more realistic than the damage evolution predicted with the micro-mechanical model. In the DSID model, damage during the second loading cycle initiates when the stress reaches the maximum stress value reached during the first cycle. In the simulations done with the DEWCD model, damage during the second loading cycle initiates at a lower stress value than the maximum stress value reached during the first cycle. The DEWCD model is the only model amongst the three tested that can capture this hysteretic effect.

4. Conclusion

The Discrete Equivalent Wing Crack Damage (DEWCD) model formulated in this paper couples micro-mechanics and Continuum Damage Mechanics (CDM) principles to study brittle materials like rocks, ceramics and concrete. In this study, we focus on the following complex features: (1) A non-linear stress/strain relationship; (2) Damage-induced anisotropy of stiffness; (3) The occurrence of irreversible strains due to volume dilation; (4) A reduction of strength after the peak stress has been reached (softening) ; (5) An apparent increase of strength and ductility in compression when the confinement increases; (6) Increasing hysteresis on unloading-reloading paths as damage increases; (7) Unilateral effects and partial recovery of stiffness in compression; (8) Different mechanical responses in tension and compression.

The Representative Elementary Volume (REV) considered in the DEWCD model is a unit sphere which is discretized with 42 integration points (to represent 42 possible micro-crack plane orientations). The REV free enthalpy is the sum of the elastic deformation energy stored in the undamaged matrix and the potential deformation energy due to the relative displacement of crack faces. Cracks are represented by penny-shaped inclusions. Damage at the REV scale is obtained by integrating the crack densities over the unit sphere. The damage yield criterion is expressed at the microscopic scale: if a crack is in tension, crack growth is controlled by a mode I fracture mechanics criterion; if a crack is in compression, the shear stress that applies at its faces is projected on the 42 directions considered in the numerical integration scheme, and cracks perpendicular to these projected force components grow according to a mode I fracture mechanics criterion. The projection

of shear stresses into a set of tensile forces allows predicting the occurrence of wing cracks at the tips of pre-existing defects subject to mode II failure. We assume that all the resulting mode I cracks do not interact and we use a dilute homogenization scheme. A hardening law is introduced to account for subcritical crack propagation, and non-associate flow rules are adopted for damage and irreversible strains induced by residual crack displacements after unloading. The DEWCD model is calibrated and validated against triaxial compression tests performed on Bakken Shale in ConocoPhillips rock mechanics laboratory.

In order to highlight the advantages of the DEWCD model over previous anisotropic damage models proposed for rocks, we simulated: (a) A uniaxial tension followed by unloading and reloading in compression; and (b) Uniaxial compression loading cycles of increasing amplitude. We compared the results obtained with the DEWCD model with those obtained with a micro-mechanical model and with a CDM model, both calibrated against the same experimental dataset as the DEWCD model. The three models predict a non linear-stress/strain relationship and damage-induced anisotropy (1)-(2). The micro-mechanical model can capture unilateral effects (7) but not the phenomena (3)-(6). The DSID model can capture the occurrence of irreversible strains (3), but cannot capture phenomena (4)-(7). The DEWCD model can capture all phenomena (1)-(8) except the softening behavior (4), which characterizes the mechanical response in case of crack interaction (beyond the scope of the present study). Note in particular that the DEWCD model is the only of the three models tested that provides realistic values of yield stress and strength in tension and compression (8). This is a significant

advancement in the theoretical modeling of rock brittle behavior, because unified models of tension and compression failure proposed so far could not distinguish properly the difference of behavior of materials in tension and compression.

The micro-mechanical model used for comparison is based on the same discrete formulation of the free enthalpy as the DEWCD model, but does not account for wing crack propagation. The CDM model used for comparison depends on the same phenomenological variables as the DEWCD model (second-order damage tensor, irreversible strains). Therefore, the numerical benchmark presented in this paper is representative and can be used to assess the relative performance of the three models. The DEWCD model proved to over-perform previous formulations purely based on micro-mechanics or purely based on CDM. Moreover, the DEWCD model depends on only 6 constitutive parameters which all have a sound physical meaning and can be determined by direct measurements in the laboratory. Future work will be devoted to the prediction of crack coalescence and to the modeling of the material response with interacting micro-cracks.

Acknowledgements

Financial support for this research was provided by ConocoPhillips and by the Offices of the Executive Vice President for Research and the Provost Georgia Tech Fund for Innovation in Research and Education (GT-FIRE).

References

Amendt, D., Busetti, S., Wenning, Q., et al., 2013. Mechanical characterization in unconventional reservoirs: A facies-based methodology. Petrophysics 54 (05), 457–464.

Arson, C., 2014. Generalized stress variables in continuum damage mechanics. Mechanics Research Communications 60, 81–84.

Ashby, M. F., Hallam, S., 1986. The failure of brittle solids containing small cracks under compressive stress states. Acta Metallurgica 34 (3), 497–510.

Bažant, P., Oh, B., 1986. Efficient numerical integration on the surface of a sphere. ZAMM-Journal of Applied Mathematics and Mechanics/Zeitschrift für Angewandte Mathematik und Mechanik 66 (1), 37–49.

Bombolakis, E., Brace, W., 1963. A note on brittle crack growth in compression. J. geophys. Res 68, 3709–3713.

Budiansky, B., O'connell, R. J., 1976. Elastic moduli of a cracked solid. International Journal of Solids and Structures 12 (2), 81–97.

Byrd, R. H., Gilbert, J. C., Nocedal, J., 2000. A trust region method based on interior point techniques for nonlinear programming. Mathematical Programming 89 (1), 149–185.

Chaboche, J.-L., 1993. Development of continuum damage mechanics for elastic solids sustaining anisotropic and unilateral damage. International Journal of Damage Mechanics 2 (4), 311–329.

Collins, I., Houlsby, G., 1997. Application of thermomechanical principles to the modelling of geotechnical materials. In: Proceedings of the Royal Society of London A: Mathematical, Physical and Engineering Sciences. Vol. 453. The Royal Society, pp. 1975–2001.

Comi, C., Perego, U., 2001. Fracture energy based bi-dissipative damage model for concrete. International Journal of Solids and Structures 38 (36), 6427–6454.

Dormieux, L., Kondo, D., Ulm, F.-J., 2006. Microporomechanics. John Wiley & Sons.

Dragon, A., Halm, D., Désoyer, T., 2000. Anisotropic damage in quasi-brittle solids: modelling, computational issues and applications. Computer methods in applied mechanics and engineering 183 (3), 331–352.

Dyskin, A., Salganik, R., 1987. Model of dilatancy of brittle materials with cracks under compression. Mechanics of solids 22 (6), 165–173.

Ehret, A., Itskov, M., Schmid, H., 2010. Numerical integration on the sphere and its effect on the material symmetry of constitutive equations—a comparative study. International journal for numerical methods in engineering 81 (2), 189–206.

Eshelby, J. D., 1957. The determination of the elastic field of an ellipsoidal inclusion, and related problems. In: Proceedings of the Royal Society of London A: Mathematical, Physical and Engineering Sciences. Vol. 241. The Royal Society, pp. 376–396.

Frémond, M., Nedjar, B., 1996. Damage, gradient of damage and principle of virtual power. International Journal of Solids and Structures 33 (8), 1083–1103.

Gambarotta, L., Lagomarsino, S., 1993. A microcrack damage model for brittle materials. International Journal of Solids and Structures 30 (2), 177–198.

Germanovich, L., Salganik, R., Dyskin, A., Lee, K., 1994. Mechanisms of brittle fracture of rock with pre-existing cracks in compression. Pure and Applied Geophysics 143 (1-3), 117–149.

Halm, D., Dragon, A., 1996. A model of anisotropic damage by mesocrack growth; unilateral effect. International Journal of Damage Mechanics 5 (4), 384–402.

Halm, D., Dragon, A., 1998. An anisotropic model of damage and frictional sliding for brittle materials. European Journal of Mechanics-A/Solids 17 (3), 439–460.

Hayakawa, K., Murakami, S., 1997. Thermodynamical modeling of elastic-plastic damage and experimental validation of damage potential. International Journal of damage mechanics 6 (4), 333–363.

Horii, H., Nemat-Nasser, S., 1983. Overall moduli of solids with microcracks: load-induced anisotropy. Journal of the Mechanics and Physics of Solids 31 (2), 155–171.

Horii, H., Nemat-Nasser, S., 1986. Brittle failure in compression: splitting, faulting and brittle-ductile transition. Philosophical Transactions of the

Royal Society of London A: Mathematical, Physical and Engineering Sciences 319 (1549), 337–374.

Jin, W., Xu, H., Arson, C., 2015. Finite element simulation of anisotropic damage around pressurized boreholes in prefractured shale.

Jin, W., Xu, H., Arson, C., Busetti, S., 2016. Computational model coupling mode ii discrete fracture propagation with continuum damage zone evolution. International Journal for Numerical and Analytical Methods in Geomechanics.

Ju, J., 1989. On energy-based coupled elastoplastic damage theories: constitutive modeling and computational aspects. International Journal of Solids and structures 25 (7), 803–833.

Kachanov, M., 1992. Effective elastic properties of cracked solids: critical review of some basic concepts. Applied Mechanics Reviews 45 (8), 304–335.

Kachanov, M., 1993. Elastic solids with many cracks and related problems.

Kachanov, M. L., 1982a. A microcrack model of rock inelasticity part i: Frictional sliding on microcracks. Mechanics of Materials 1 (1), 19–27.

Kachanov, M. L., 1982b. A microcrack model of rock inelasticity part ii: propagation of microcracks. Mechanics of Materials 1 (1), 29–41.

Kachanov, M. L., Shafiro, B., Tsukrov, I., 2013. Handbook of elasticity solutions. Springer Science & Business Media.

Krajcinovic, D., Basista, M., Sumarac, D., 1991. Micromechanically inspired phenomenological damage model. Journal of Applied Mechanics 58 (2), 305–310.

Lehner, F., Kachanov, M., 1996. On modelling of 'winged" cracks forming under compression. International Journal of Fracture 77 (4), R69–R75.

Levasseur, S., Collin, F., Charlier, R., Kondo, D., 2013. On micromechanical damage modeling in geomechanics: Influence of numerical integration scheme. Journal of Computational and Applied Mathematics 246, 215–224.

Lubarda, V., Krajcinovic, D., Mastilovic, S., 1994. Damage model for brittle elastic solids with unequal tensile and compressive strengths. Engineering Fracture Mechanics 49 (5), 681–697.

Mazars, J., Berthaud, Y., Ramtani, S., 1990. The unilateral behaviour of damaged concrete. Engineering Fracture Mechanics 35 (4), 629–635.

Murakami, S., 1988. Mechanical modeling of material damage. Journal of Applied Mechanics 55 (2), 280–286.

Murakami, S., 2012. Continuum damage mechanics: a continuum mechanics approach to the analysis of damage and fracture. Vol. 185. Springer.

Nemat-Nasser, S., Horii, H., 1982. Compression-induced nonplanar crack extension with application to splitting, exfoliation, and rockburst. Journal of Geophysical Research: Solid Earth (1978–2012) 87 (B8), 6805–6821.

Nemat-Nasser, S., Obata, M., 1988. A microcrack model of dilatancy in brittle materials. Journal of applied mechanics 55 (1), 24–35.

Paliwal, B., Ramesh, K., 2008. An interacting micro-crack damage model for failure of brittle materials under compression. Journal of the Mechanics and Physics of Solids 56 (3), 896–923.

Pensee, V., Kondo, D., 2003. Micromechanics of anisotropic brittle damage: comparative analysis between a stress based and a strain based formulation. Mechanics of materials 35 (8), 747–761.

Pensée, V., Kondo, D., Dormieux, L., 2002. Micromechanical analysis of anisotropic damage in brittle materials. Journal of Engineering Mechanics 128 (8), 889–897.

Qi, M., Shao, J., Giraud, A., Zhu, Q., Colliat, J., 2016a. Damage and plastic friction in initially anisotropic quasi brittle materials. International Journal of Plasticity 82, 260–282.

Qi, M., Shao, J., Giraud, A., Zhu, Q., Colliat, J., 2016b. A numerical damage model for initially anisotropic materials. International Journal of Solids and Structures 100–101 (245–256).

Sahouryeh, E., Dyskin, A., Germanovich, L., 2002. Crack growth under biaxial compression. Engineering Fracture Mechanics 69 (18), 2187–2198.

Savalli, L., Engelder, T., 2005. Mechanisms controlling rupture shape during subcritical growth of joints in layered rocks. Geological Society of America Bulletin 117 (3-4), 436–449.

Scholtès, L., Donzé, F.-V., 2012. Modelling progressive failure in fractured rock masses using a 3d discrete element method. International Journal of Rock Mechanics and Mining Sciences 52, 18–30.

Shao, J.-F., Chau, K., Feng, X., 2006. Modeling of anisotropic damage and creep deformation in brittle rocks. International journal of rock mechanics and mining sciences 43 (4), 582–592.

Shao, J. F., Rudnicki, J., 2000. A microcrack-based continuous damage model for brittle geomaterials. Mechanics of Materials 32 (10), 607–619.

Shao, J.-F., Zhou, H., Chau, K., 2005. Coupling between anisotropic damage and permeability variation in brittle rocks. International Journal for Numerical and Analytical Methods in Geomechanics 29 (12), 1231–1247.

Simo, J., Ju, J., 1987. Strain-and stress-based continuum damage models—i. formulation. International journal of solids and structures 23 (7), 821–840.

Sone, H., Zoback, M. D., 2013a. Mechanical properties of shale-gas reservoir rocks—part 1: Static and dynamic elastic properties and anisotropy. Geophysics 78 (5), D381–D392.

Sone, H., Zoback, M. D., 2013b. Mechanical properties of shale-gas reservoir rocks—part 2: Ductile creep, brittle strength, and their relation to the elastic modulus. Geophysics 78 (5), D393–D402.

Waltz, R. A., Morales, J. L., Nocedal, J., Orban, D., 2006. An interior algorithm for nonlinear optimization that combines line search and trust region steps. Mathematical Programming 107 (3), 391–408.

Xu, H., Arson, C., 2014. Anisotropic damage models for geomaterials: theoretical and numerical challenges. International Journal of Computational Methods 11 (02), 1342007.

Xu, H., Arson, C., 2015. Mechanistic analysis of rock damage anisotropy and rotation around circular cavities. Rock Mechanics and Rock Engineering, 1–17.

Yuan, S., Harrison, J., 2006. A review of the state of the art in modelling progressive mechanical breakdown and associated fluid flow in intact heterogeneous rocks. International Journal of Rock Mechanics and Mining Sciences 43 (7), 1001–1022.

Zhu, C., Arson, C., 2013. A thermo-mechanical damage model for rock stiffness during anisotropic crack opening and closure. Acta Geotechnica, 1–21.

Zhu, Q., Kondo, D., Shao, J., 2008. Micromechanical analysis of coupling between anisotropic damage and friction in quasi brittle materials: role of the homogenization scheme. International Journal of Solids and Structures 45 (5), 1385–1405.

Zhu, Q., Kondo, D., Shao, J.-F., 2009. Homogenization-based analysis of anisotropic damage in brittle materials with unilateral effect and interactions between microcracks. International Journal for Numerical and Analytical Methods in Geomechanics 33 (6), 749–772.

Zhu, Q., Shao, J.-F., 2015. A refined micromechanical damage–friction model with strength prediction for rock-like materials under compression. International Journal of Solids and Structures 60, 75–83.

Table 1: DEWCD parameters calibrated for Bakken Shale

Elasticity		Initial State		Damage function	
E_0	ν_0	a_0	$\mathbb{N}$	K_0	σ_c
GPa	$-$	L	N/L^3	$MPa/LMPa$	
40.8	0.32	0.022	960	3.6	1×10^4

Table 2: Theoretical formulation of the micro-mechanical damage model

Micromechanical Damage Model	
Free Energy	$G = \frac{1}{2}\boldsymbol{\sigma} : \mathbb{S}_0 : \boldsymbol{\sigma} + \frac{1}{2}\sum_{i=1}^{M} w_i\{c_0\rho_i(\overrightarrow{n_i}\cdot\boldsymbol{\sigma}\cdot\overrightarrow{n_i})\langle\overrightarrow{n_i}\cdot\boldsymbol{\sigma}\cdot\overrightarrow{n_i}\rangle^+ +$ $c_1\rho_i[(\boldsymbol{\sigma}\cdot\boldsymbol{\sigma}) : (\overrightarrow{n_i}\otimes\overrightarrow{n_i}) - \boldsymbol{\sigma} : (\overrightarrow{n_i}\otimes\overrightarrow{n_i}\otimes\overrightarrow{n_i}\otimes\overrightarrow{n_i}) : \boldsymbol{\sigma}]\}$ $\boldsymbol{\varepsilon} = \frac{\partial G_s}{\partial\boldsymbol{\sigma}} = \frac{1+\nu_0}{E_0}\boldsymbol{\sigma} - \frac{\nu_0}{E_0}(\mathrm{Tr}\boldsymbol{\sigma})\,\boldsymbol{\delta} + \sum_{i=1}^{M} w_i\{c_0\rho_i\langle\overrightarrow{n_i}\cdot\boldsymbol{\sigma}\cdot\overrightarrow{n_i}\rangle^+\overrightarrow{n_i}\otimes\overrightarrow{n_i}$ $+c_1\rho_i[\boldsymbol{\sigma}\cdot(\overrightarrow{n_i}\otimes\overrightarrow{n_i}) - (\overrightarrow{n_i}\cdot\boldsymbol{\sigma}\cdot\overrightarrow{n_i})\overrightarrow{n_i}\otimes\overrightarrow{n_i}]\}$ $Y_i = \frac{1}{2}\frac{\partial G_s}{\partial\rho_i} = w_i\{c_0(\overrightarrow{n_i}\cdot\boldsymbol{\sigma}\cdot\overrightarrow{n_i})\langle\overrightarrow{n_i}\cdot\boldsymbol{\sigma}\cdot\overrightarrow{n_i}\rangle^+$ $+c_1[(\boldsymbol{\sigma}\cdot\boldsymbol{\sigma}) : (\overrightarrow{n_i}\otimes\overrightarrow{n_i}) - \boldsymbol{\sigma} : (\overrightarrow{n_i}\otimes\overrightarrow{n_i}\otimes\overrightarrow{n_i}\otimes\overrightarrow{n_i}) : \boldsymbol{\sigma}]\}$
Damage Criteria	$f_d(n_i, Y_i, \rho_i) = Y_i - k(1+\eta\rho_i)$
Flow Rule	$\dot{\rho}_i = \dot{\lambda}_i\frac{\partial f_d(n_i,Y_i,\rho_i)}{\partial Y_i} = \dot{\lambda}_i$ $\dot{\lambda}_i = \frac{Y_i}{k\eta} = \frac{1}{k\eta}\frac{\partial Y_i}{\partial\boldsymbol{\sigma}} : \dot{\boldsymbol{\sigma}}$ $\frac{\partial Y_i}{\partial\boldsymbol{\sigma}} = w_i\{c_0\langle\overrightarrow{n_i}\cdot\boldsymbol{\sigma}\cdot\overrightarrow{n_i}\rangle^+\overrightarrow{n_i}\otimes\overrightarrow{n_i}$ $+c_1[\boldsymbol{\sigma}\cdot(\overrightarrow{n_i}\otimes\overrightarrow{n_i}) - (\overrightarrow{n_i}\cdot\boldsymbol{\sigma}\cdot\overrightarrow{n_i})\overrightarrow{n_i}\otimes\overrightarrow{n_i}]\}$

G: Free enthalpy	$\boldsymbol{\varepsilon}$: Total strain	k: Initial damage threshold
$\boldsymbol{\sigma}$: Stress tensor	$\boldsymbol{\delta}$: Kronecker delta	$\mathbb{S}_0$: Undamaged compliance tensor
ρ_i: Damage density	Y_i: Damage driving force	$\dot{\rho}_i$: Damage density rate
E_0: Young's Modulus	ν_0: Poisson's ratio	η: Damage hardening variable
f_d: Damage function	$\dot{\lambda}_i$: Lagrangian Multiplier	w_i: Weight in direction $\overrightarrow{n_i}$

Table 3: Micromechanical damage model parameters calibrated for Bakken Shale

Elasticity		Initial State		Damage function	
E_0	ν_0	a_0	$\mathbb{N}$	k	η
GPa	$-$	L	N/L^3	J/L^3	J/L^3
53.5	0.35	0.050	960	278.9	116.6

Table 4: Theoretical formulation of the DSID model

D.S.I.D. Model	
Free Energy	$G(\boldsymbol{\sigma},\boldsymbol{\Omega}) = \frac{1}{2}\boldsymbol{\sigma} : \mathbb{S}_0 : \boldsymbol{\sigma} + a_1\,\mathrm{Tr}\boldsymbol{\Omega}(\mathrm{Tr}\boldsymbol{\sigma})^2 + a_2\,\mathrm{Tr}(\boldsymbol{\sigma}\cdot\boldsymbol{\sigma}\cdot\boldsymbol{\Omega}) + a_3\,\mathrm{Tr}\boldsymbol{\sigma}\,\mathrm{Tr}(\boldsymbol{\Omega}\cdot\boldsymbol{\sigma}) + a_4\,\mathrm{Tr}\boldsymbol{\Omega}\,\mathrm{Tr}(\boldsymbol{\sigma}\cdot\boldsymbol{\sigma})$ $\boldsymbol{\varepsilon}^E = \frac{\partial G}{\partial \boldsymbol{\sigma}} = \frac{1+\nu_0}{E_0}\boldsymbol{\sigma} - \frac{\nu_0}{E_0}(\mathrm{Tr}\boldsymbol{\sigma})\,\boldsymbol{\delta} + 2a_1(\mathrm{Tr}\boldsymbol{\Omega}\,\mathrm{Tr}\boldsymbol{\sigma})\,\boldsymbol{\delta} + a_2(\boldsymbol{\sigma}\cdot\boldsymbol{\Omega}+\boldsymbol{\Omega}\cdot\boldsymbol{\sigma}) + a_3[\,\mathrm{Tr}(\boldsymbol{\sigma}\cdot\boldsymbol{\Omega})\,\boldsymbol{\delta} + (\mathrm{Tr}\boldsymbol{\sigma})\,\boldsymbol{\Omega}\,] + 2a_4(\mathrm{Tr}\boldsymbol{\Omega})\,\boldsymbol{\sigma}$ $\boldsymbol{Y} = \frac{\partial G}{\partial \boldsymbol{\Omega}} = a_1(\mathrm{Tr}\boldsymbol{\sigma})^2\,\boldsymbol{\delta} + a_2\boldsymbol{\sigma}\cdot\boldsymbol{\sigma} + a_3\mathrm{Tr}(\boldsymbol{\sigma})\boldsymbol{\sigma} + a_4\mathrm{Tr}(\boldsymbol{\sigma}\cdot\boldsymbol{\sigma})\boldsymbol{\delta}$
Damage Function	$f_d = \sqrt{J^*} - \alpha I^* - k$ $J^* = \frac{1}{2}(\mathbb{P}_1 : \boldsymbol{Y} - \frac{1}{3}I^*\boldsymbol{\delta}) : (\mathbb{P}_1 : \boldsymbol{Y} - \frac{1}{3}I^*\boldsymbol{\delta}), \quad I^* = (\mathbb{P}_1 : \boldsymbol{Y}) : \boldsymbol{\delta}$ $\mathbb{P}_1(\boldsymbol{\sigma}) = \sum_{p=1}^{3}\left[H(\sigma^{(p)}) - H(-\sigma^{(p)})\right]\boldsymbol{n}^{(p)}\otimes\boldsymbol{n}^{(p)}\otimes\boldsymbol{n}^{(p)}\otimes\boldsymbol{n}^{(p)}$ $k = C_0 - C_1\mathrm{Tr}(\boldsymbol{\Omega})$
Damage Potential	$g_d = \sqrt{\frac{1}{2}(\mathbb{P}_2 : \boldsymbol{Y}) : (\mathbb{P}_2 : \boldsymbol{Y})}$ $\mathbb{P}_2 = \sum_{p=1}^{3} H\left[\max_{q=1}^{3}(\sigma^{(q)}) - \sigma^{(p)}\right]\boldsymbol{n}^{(p)}\otimes\boldsymbol{n}^{(p)}\otimes\boldsymbol{n}^{(p)}\otimes\boldsymbol{n}^{(p)}$
Flow Rule	$\dot{\boldsymbol{\varepsilon}}^{id} = \dot{\lambda}_d\frac{\partial f_d}{\partial \boldsymbol{\sigma}} = \dot{\lambda}_d\frac{\partial f_d}{\partial \boldsymbol{Y}} : \frac{\partial \boldsymbol{Y}}{\partial \boldsymbol{\sigma}}$ $\dot{\boldsymbol{\Omega}} = \dot{\lambda}_d\frac{\partial g_d}{\partial \boldsymbol{Y}}$

G: Gibbs free energy	$\boldsymbol{\varepsilon}^E$: Total elastic strain	C_0: Initial damage threshold
$\boldsymbol{\sigma}$: Stress tensor	$\boldsymbol{\delta}$: Kronecker delta	$\mathbb{S}_0$: Undamaged compliance tensor
$\boldsymbol{\Omega}$: Damage variable	$\boldsymbol{Y}$: Damage driving force	max$(\cdot)$: Maximum function
E_0: Young's Modulus	$\dot{\boldsymbol{\Omega}}$: Damage rate	C_1: Damage hardening variable
ν_0: Poisson's ratio	$H(\cdot)$: Heaviside function	a_1, a_2, a_3, a_4: Material parameters
f_d: Damage function	$\dot{\lambda}_d$: Lagrangian Multiplier	$\mathbb{P}_1$ and $\mathbb{P}_2$: Projection tensors
g_d: Damage potential	$\dot{\boldsymbol{\varepsilon}}^{id}$: Irreversible strain rate	$\sigma^{(p)}$; $\boldsymbol{n}^{(p)}$: Principal stress tensor, vector

Table 5: DSID parameters calibrated for Bakken shale

Elasticity		Free Energy				Damage function		
E_0	ν_0	a_1	a_2	a_3	a_4	C_0	C_1	α
GPa	$-$	MPa^{-1}	MPa^{-1}	MPa^{-1}	MPa^{-1}	MPa	MPa	$-$
46	0.186	7.35×10^{-7}	1.21×10^{-4}	-3.15×10^{-11}	2.39×10^{-12}	0.01	1.18	0.399

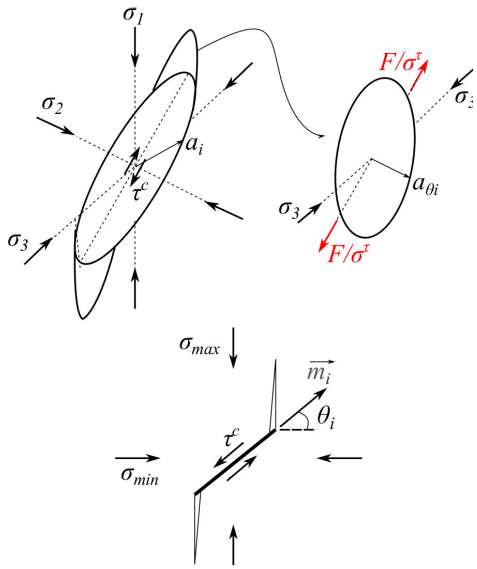

Figure 1: Wing crack propagation model in 3D under compression.

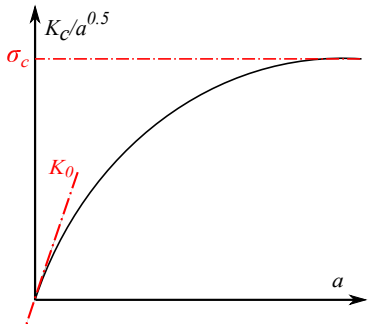

Figure 2: Hyperbolic damage hardening function used in the DEWCD model

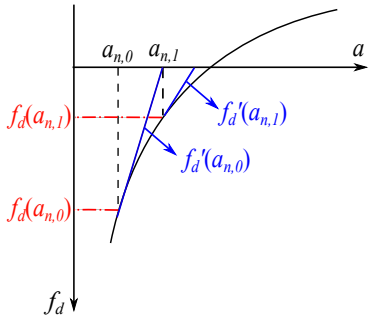

Figure 3: Newton iteration scheme used to calculate the Lagrange multiplier with the hyperbolic hardening law used in the proposed model

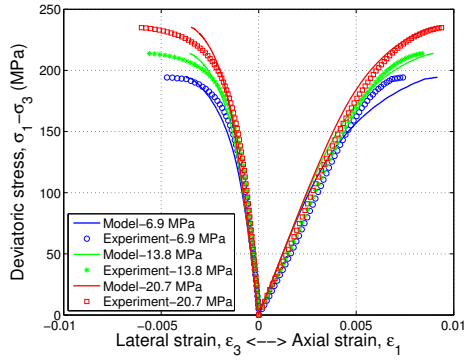

(a) Calibration and validation of DEWCD model stress/strain curves

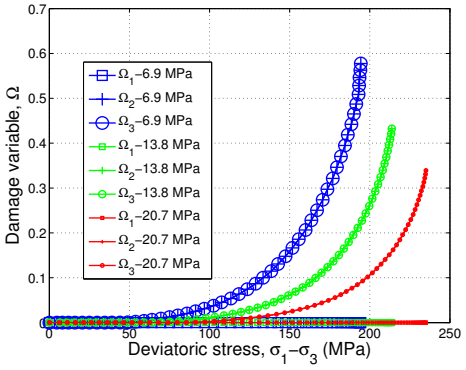

(b) Prediction of damage with the DEWCD model

Figure 4: Calibration and validation of the DEWCD model parameters against experimental stress-strain curves obtained during triaxial compression tests under various confining pressures. (a) Triaxial data with a confining pressure $\sigma_3 = 13.8$MPa is used to calibrate the model. Triaxial datasets for confining pressures of $\sigma_3 = 6.9$MPa and $\sigma_3 = 20.7$MPa are employed to validate the calibration. (b) Evolution of the three principal values of the damage tensor with the calibrated parameters, for the three confining pressures.

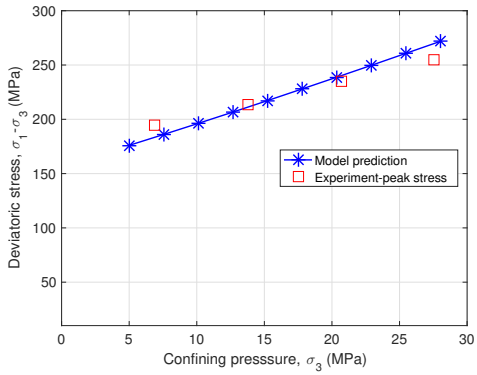

Figure 5: Variations of the stress at which the Young's modulus is reduced to 25% of its reference (initial) value with the confining pressure. Comparison of DEWCD model predictions with the peak stress (strength) obtained experimentally in shale.

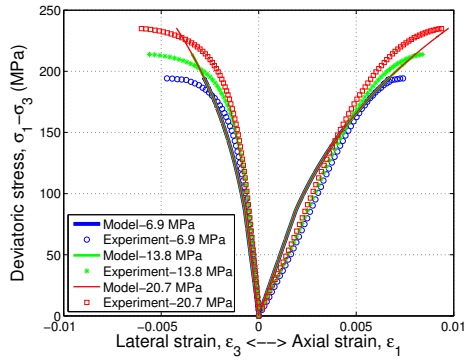

(a) Calibration and validation of micromechanical model stress/strain curves

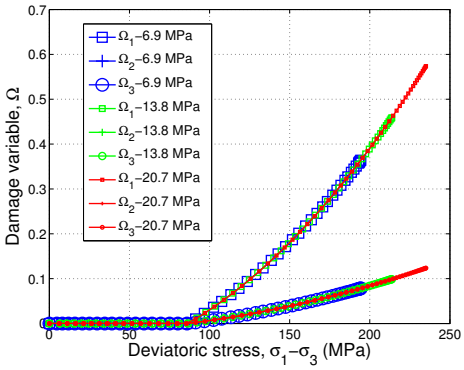

(b) Prediction of damage with the micromechanical model

Figure 6: Calibration and validation of the micromechanical damage model against triaxial compression tests performed on Bakken Shale. (a) Stress/strain curves (calibration based on data obtained at 13.8 MPa confinement, and verification against tests performed under confining stresses of 6.9 MPa and 20.7 MPa). (b) Evolution of the three principal values of damage during the tests.

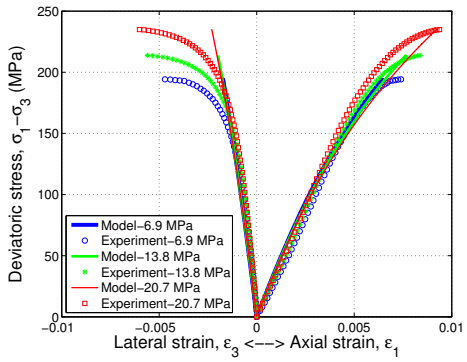

(a) Calibration and validation of DSID model stress/strain curves

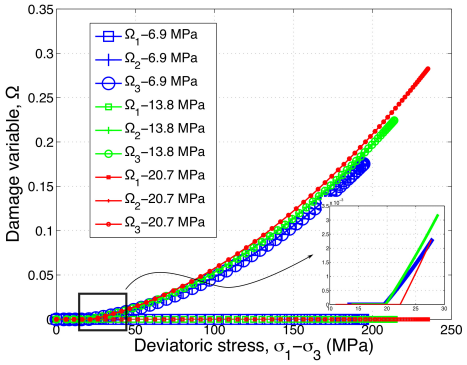

(b) Prediction of damage with the DSID model

Figure 7: Calibration and validation of the DSID model against triaxial compression tests performed on Bakken Shale. (a) Stress/strain curves (calibration based on data obtained at 13.8 MPa confinement, and verification against tests performed under confining stresses of 6.9 MPa and 20.7 MPa). (b) Evolution of the three principal values of damage during the tests.

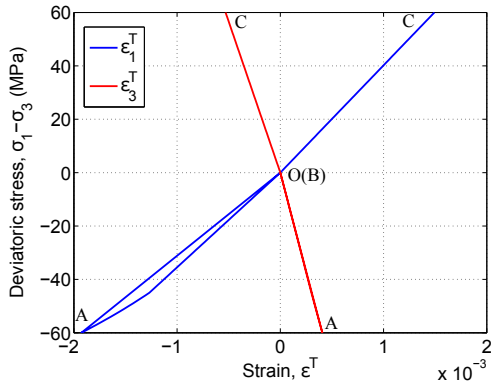

(a) Stress/strain curve predicted with the micro-mechanical model

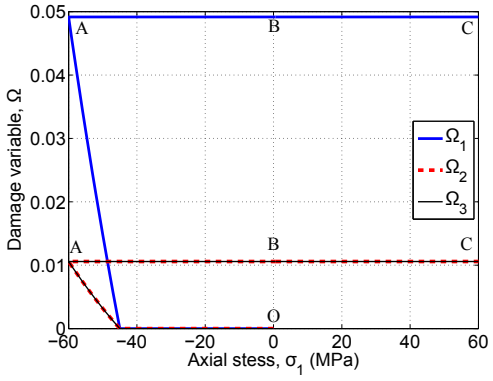

(b) Damage evolution predicted with the micro-mechanical model

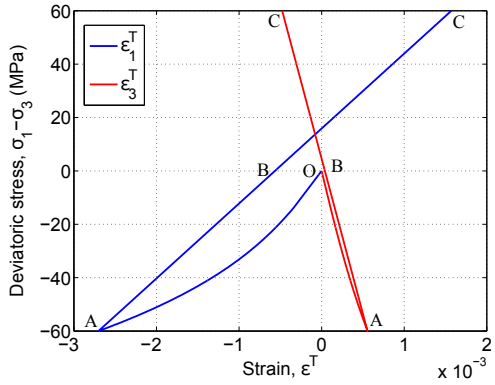

(c) Stress/strain curve predicted with the DSID model

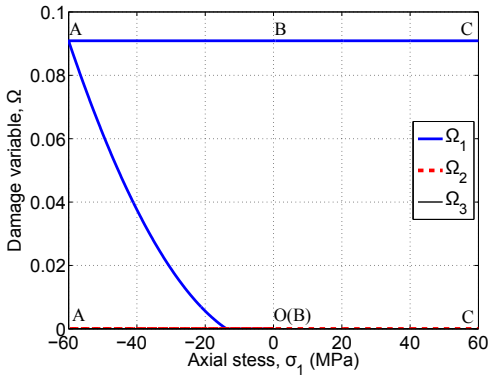

(d) Damage evolution predicted with the DSID model

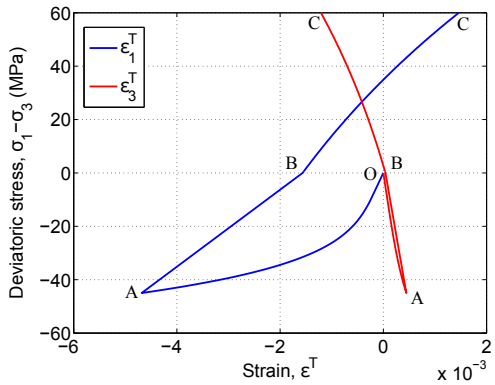

(e) Stress/strain curve predicted with the DEWCD model

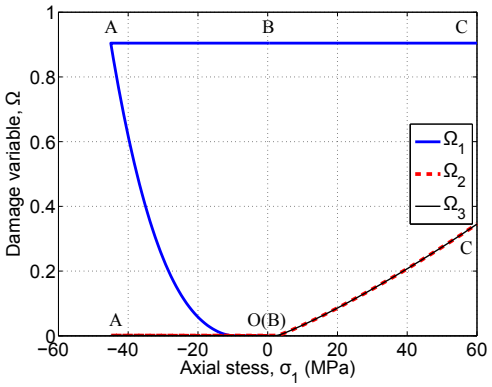

(f) Damage evolution predicted with the DEWCD model

Figure 8: Comparison of the stress-strain behavior and damage evolution predicted the micro-mechanical, DSID and DEWCD models, for a stress path that comprises a uniaxial tension (OA), an elastic compressive unloading (AB), followed by an inelastic compressive loading (BC). The three models were calibrated against the same experimental data.

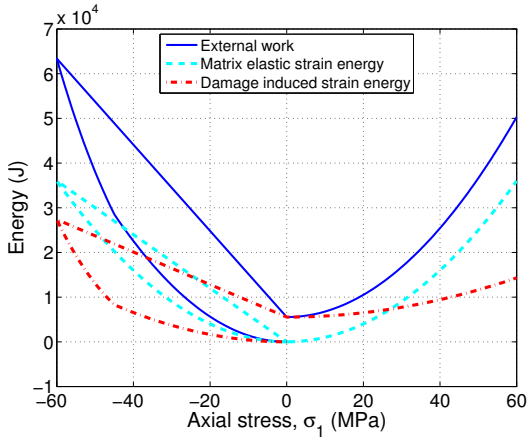

(a) Energy evolution - micro-mechanical model

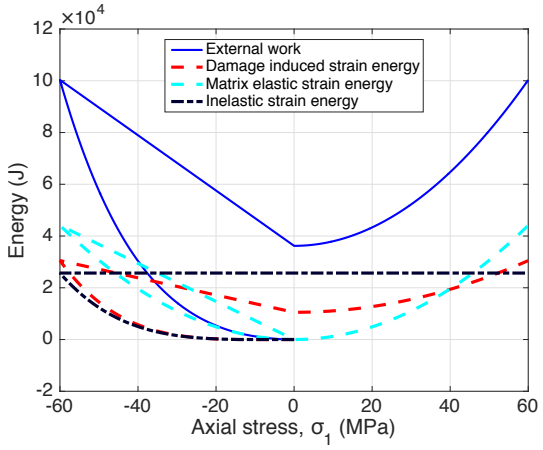

(b) Energy evolution - DSID model

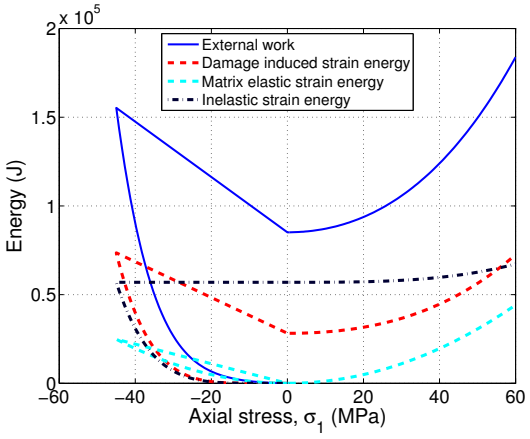

(c) Energy evolution - DEWCD model

Figure 9: Evolution of the energy potentials during the simulation of uniaxial tension followed by unloading and compressive reloading.

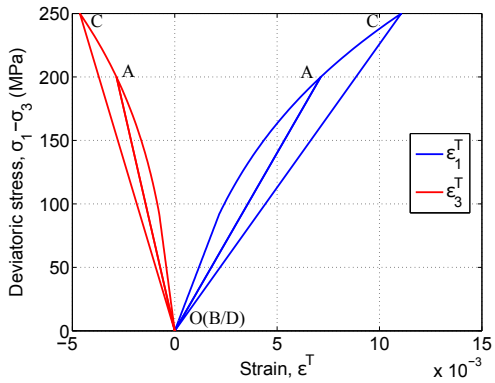

(a) Stress/strain curve predicted with the micro-mechanical model

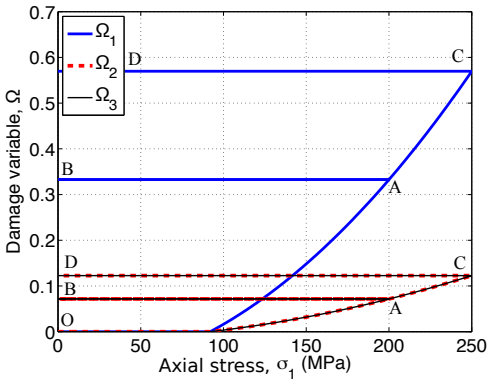

(b) Damage evolution predicted with the micro-mechanical model

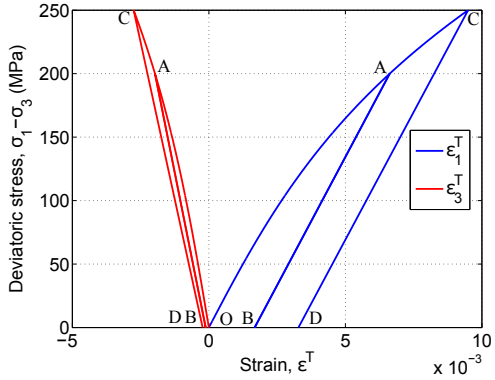

(c) Stress/strain curve predicted with the DSID model

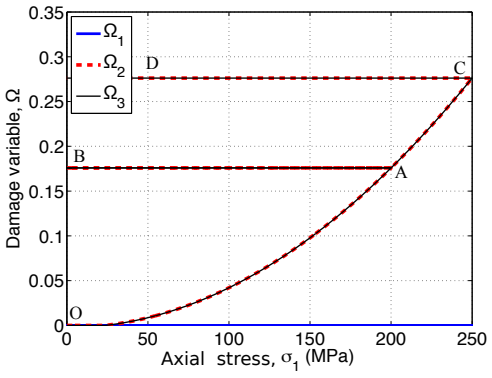

(d) Damage evolution predicted with the DSID model

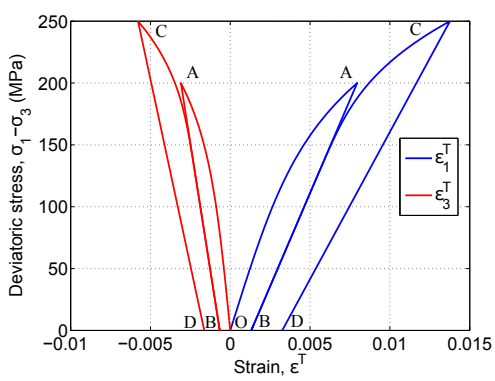

(e) Stress/strain curve predicted with the DEWCD model

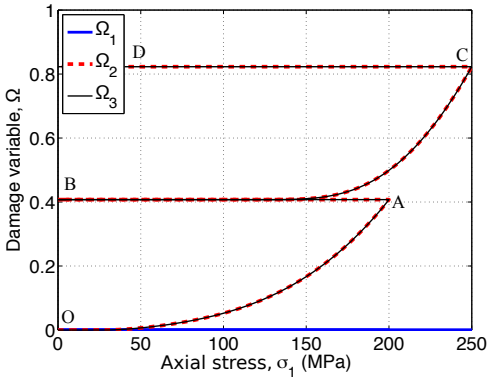

(f) Damage evolution predicted with the DEWCD model

Figure 10: Comparison of the stress-strain behavior and damage evolution predicted the micro-mechanical, DSID and DEWCD models, for a stress path that comprises two cycles of uniaxial compression loading - elastic unloading. The three models were calibrated against the same experimental data.